ADVANCED FUNCTIONAL MATERIALS
www.afm-journal.de

Materials Views
www.MaterialsViews.com

# Excellent Field-Emission Performances of Neodymium Hexaboride ($NdB_6$) Nanoneedles with Ultra-Low Work Functions

*Junqi Xu, Guanghua Hou, Takao Mori, Huiqiao Li, Yanrui Wang, Yangyang Chang, Yongsong Luo, Benhai Yu, Ying Ma, and Tianyou Zhai**

**High-quality $NdB_6$ nanostructures with a low work function are successfully synthesized via an one-step catalyst-free chemical vapor deposition process. Field emission properties of these nanostructures (curve nanowires, short-straight nanorods, long-straight nanowires, and nanoneedles) are systematically investigated and found to be strongly affected by the tip morphologies and temperatures. The nanoneedles with sharp tips demonstrate the lowest turn-on (2.71 V/μm) and threshold (3.60 V/μm) electric fields, as well as a high current density (5.37 mA/cm$^2$) at a field of 4.32 V/μm in comparision with other nanostructures. Furthermore, with an increase in temperature from room temperature to 623 K, the turn-on field of the nanoneedles decreases from 2.71 to 1.76 V/μm, and the threshold field decreases from 3.60 to 2.57 V/μm. Such excellent performances make $NdB_6$ nanomaterials promising candidates for application in flat panel displays and nanoelectronics building blocks.**

## 1. Introduction

One-dimensional micro/nanoscale materials have drawn tremendous attention due to their basic scientific research and potential technological applications.[1] Field emission (FE) is based on the physical phenomenon of quantum tunneling, during which electrons are injected from a material's surface into vacuum under the influence of an applied electric field. The Fowler-Nordheim (F-N) theory predicts that electron emitters made of materials with a low work function, higher aspect ratio and higher curvature of the tip, could greatly enhance the FE current with a lower applied turn-on voltage.[2]

Rare-earth hexaboride ($REB_6$) nanostructures are ideal materials for FE application as an electrical field-induced ion and electron point source due to their miniature dimensions, low work functions, as well as excellent electrical, thermal, and mechanical properties.[3–11] The advantages of using $REB_6$ as a FE candidate originate from their crystal structure, in which the rare-earth metal atom is embedded inside a stable boron octahedral network. The boron octahedral network arrangement results in a unique combination of all the desired properties for an excellent cathode material. So far, most previous studies focused on the synthesis and FE properties of $LaB_6$ nanostructures since $LaB_6$ has the relatively low work function (2.6 eV) and good stability. Recent theoretical research showed that the cathodes materials with work functions lower than 2 eV may undergo different electron emission mechanisms, including thermionic emission, field emission, and field-induced ballistic emission, which provides us the light to improve the emission performances using these special mechanisms.[12] Neodymium hexaboride ($NdB_6$) was reported to have an ultra-low work function (1.6 eV)[13] than many previously reported FE materials (Table S1). If single-crystalline $NdB_6$ nanostructures with a high aspect ratio morphology, such as nanowires and/or nanoneedles, can be fabricated, it might be an ideal candidate for the investigation and development of advanced field emission theory, and efficient cathodes for vacuum electronic devices.

The great challenges for the fabrication of high-quality $NdB_6$ nanostructures first come from the existence of several thermodynamically stable $NdB_6$ phase with different Nd:B atoms;[14] Second, the traditional methods, such as floating zone method,[15] solid-state reaction,[16] borothermal reduction process,[17] thermal evaporation[18] and hydrothermal reaction,[19] etc. are not suitable for the growth of high-aspect-ratio $NdB_6$ nanostructures. To the best of our knowledge, there are only two literatures on $NdB_6$ nanowire synthesis: Ding et al.[20] fabricated the $NdB_6$ nanowires through a self-catalysis process,

Dr. J. Q. Xu, Prof. H. Q. Li, Prof. Y. Ma, Prof. T. Y. Zhai
State Key Laboratory of Material Processing and Die & Mould Technology
School of Material Sciences and Engineering
Huazhong University of Science and Technology (HUST)
Wuhan, 430074, PR China
E-mail: zhaity@hust.edu.cn
Prof. J. Q. Xu, G. H. Hou, Y. R. Wang, Y. Y. Chang, Prof. Y. S. Luo, Prof. B. H. Yu
Key Laboratory of Advanced Micro/Nano Functional Materials
Department of Physics and Electronic Engineering
Xinyang Normal University
Xinyang, 464000, PR China
Prof. T. Mori
International Center for Materials Nanoarchitectonics (MANA)
National Institute for Materials Science (NIMS)
Namiki 1–1, Tsukuba, Ibaraki 305–0044, Japan

DOI: 10.1002/adfm201301980

however, the lack control on growth direction and wire diameter in this method limits its further application. Recently, Cheung et al.[21] developed a palladium-nanoparticle-catalyzed chemical vapor deposition (CVD) process to synthesize $NdB_6$ nanowires and nanoobelisks, but the boron precursor ($B_{10}H_{14}$) is solid and not easy to control its flow under CVD system, in addition, this approach requires external heating devices and complex pipe lines into the reactor. Therefore, more effective and easy operable method to synthesize $NdB_6$ nanostructures should be developed. Besides of synthesis, the property and application of $NdB_6$ nanostructures has not been reported to date.

Very recently, we developed an effective CVD approach to synthesis vertically aligned single-crystalline $LaB_6$ nanowire arrays using $LaCl_3 \cdot 3H_2O$ as the La source and $B_2H_6$ as the B source.[22] Here, we extend this method to fabricate high quality and uniform 1D $NdB_6$ nanostructures with different morphologies. Through this one-step catalyst-free CVD method, $NdB_6$ nanostructures with different morphologies, such as curve nanowires, short-straight nanorods, long-straight nanowires, and nanoneedles, can be successfully obtained. The morphology of the $NdB_6$ nanostructures can be adjusted by tuning the reaction temperatures and the distances between the precursors and the substrate. The field emission properties of these nanostructures are comparatively investigated and found to be strongly affected by the morphologies. The $NdB_6$ nanoneedles with maximum curvature of radius are the best field emitters with a low turn-on field of 2.71 V/μm, a low threshold field of 3.60 V/μm, and a good stability. Besides, the temperature-dependent field emission properties of the $NdB_6$ nanoneedles are also investigated: the turn-on field, threshold field, current density, and the dependence of the effective work function on temperature are discussed for better understanding of the FE mechanism of the regarded nanoneedles.

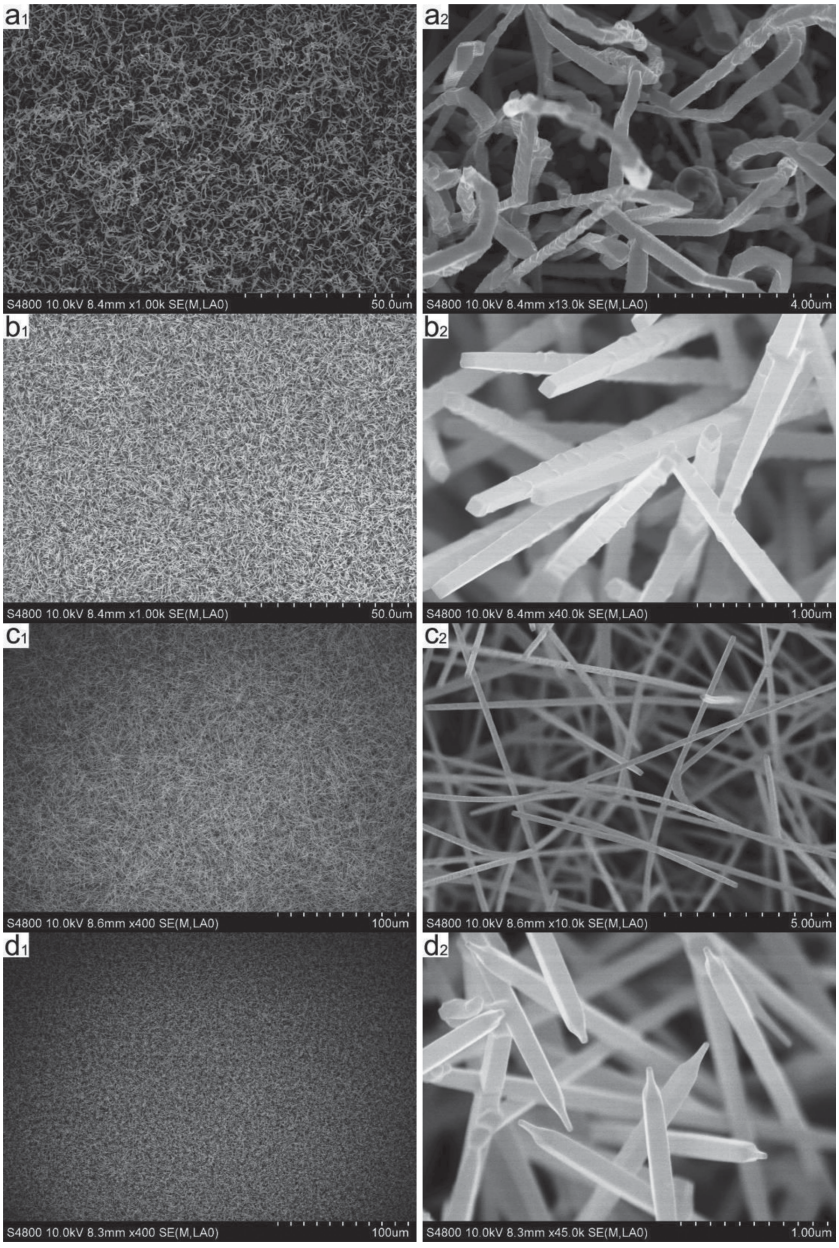


**Figure 1.** Typical SEM images of several $NdB_6$ nanostructures: a) curve nanowires (Sample **a**); b) short-straight nanorods (Sample **b**); (c) long-straight nanowires (Sample **c**); and d) nanoneedles (Sample **d**).

## 2. Results and Discussion

### 2.1. The Morphology, Structure, and Growth Mechanism of $NdB_6$ Nanostructures

Representative morphologies and structures of the produced $NdB_6$ nanostructures, as revealed by field-emission scanning electron microscopy (SEM), are shown in **Figure 1**. The low-magnification SEM images (Figures $1a_1$, $b_1$, $c_1$ and $d_1$) demonstrate that the $NdB_6$ nanostructures uniformly and compactly cover the entire substrates. The morphologies at high-magnification (shown in Figures $1a_2$, $b_2$, $c_2$ and $d_2$) are quite different depending on synthetic conditions, mainly due to the reaction temperature and distances between the precursors and the substrates. Figure 1a is the SEM image of a product obtained at a low temperature (860 °C) and a short distance (3 cm). The nanowires are curve with a diameter of ~160–200 nm and a length of ~8–10 μm. With a rise in the reaction temperature (880 °C) and at a short distance (5 cm), the morphology changes from curve to straight, and the obtained short-straight nanorods

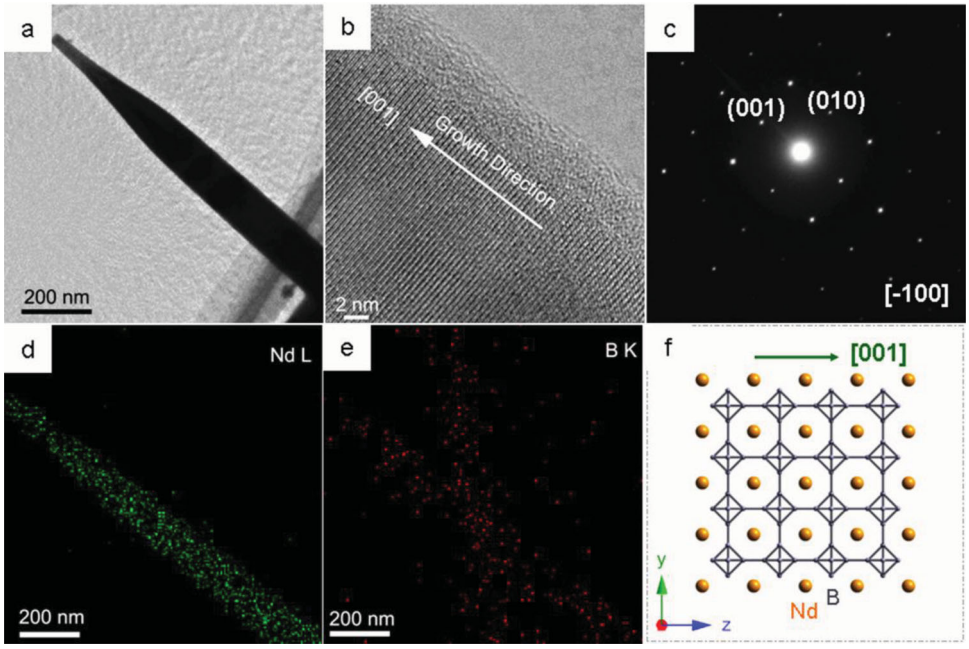


**Figure 2.** TEM images of $NdB_6$ nanoneedle: a) TEM image; b) HRTEM image; c) the corresponding SAED pattern; d) Nd elemental maps; e) B elemental maps; f) atomic model of a cubic $NdB_6$ with the [001] growth direction.

show a smaller diameter of ~140–160 nm and square cross-section (as shown in Figure 1b). On increasing the reaction temperature to 900 °C and the distance to 7 cm, long-straight nanowires with a further smaller diameter of ~120–140 nm was obtained, and the length is up to ~40–50 μm (as shown in Figure 1c). When the reaction temperature reaches 920 °C and the distance increases to 9 cm, high-density needlelike nanostructures, with a length of ~20–30 μm are observed on the whole Si wafers (as shown in Figure 1d). Magnified images of these nanoneedles taken from a different view (see Supporting Information, Figure S1) reveals that this $NdB_6$ structure has an abruptly sharpened tip, which is very favorable for the field emission. Thus, the synthesize conditions play a key role in determining the deposited $NdB_6$ morphologies.

A typical low-magnification transmission electron microscopy (TEM) image of the $NdB_6$ nanoneedle is shown in **Figure 2**a. The nanoneedle has smooth surface and sharp needle, and is ~120 nm in lateral dimension. Figure 2b is a high-resolution TEM image, which confirms that the nanoneedle is well crystallized and is parallel to the [001] crystallographic direction. A corresponding selected-area electron diffraction (SAED) pattern of the nanoneedle in Figure 2c reveals that this nanoneedle is grown in the [001] crystallographic direction of the cubic $NdB_6$ with lattice constant a = 0.41 nm. The diffraction pattern appears identical as we moved the SAED aperture along the entire nanoneedle, suggesting that the $NdB_6$ nanoneedle is single crystalline. The <001> growth of these $NdB_6$ nanoneedles may be attributed to the fact that the {001} lattice planes of the $NdB_6$ have the highest atom density, and therefore, it would minimize the total energy for the crystal to growth in this direction.[7c] Figure 2f displays a corresponding structural model, which is in good agreement with the HRTEM images of $NdB_6$ nanoneedles. A detailed chemical analysis was carried out using element mappings. Figure 2d shows the Nd elemental map and demonstrates a uniform distribution of the compositional elements Nd. However, it is difficult to accurately detect the B elements (Figure 2e) because of the small atom number. Therefore, high-quality single-crystalline $NdB_6$ nanostructures elongated preferentially [001] direction have been successfully fabricated.

The X-ray diffraction (XRD) patterns of the as-synthesized $NdB_6$ nanoneedles (sample **d**, top trace) and the standard $NdB_6$ powder diffraction pattern from the Joint Committee on Powder Diffraction Standards Card (JCPDS No. 11–0087) (bottom trace) are both presented in **Figure 3**a. No characteristic peaks of impurities are detected, indicating the high purity of the synthesized product. All the diffraction peaks can be well indexed to cubic $NdB_6$ with a lattice of a = 0.41 nm and a space group of *Pm-3m*, in good agreement with the literature values.[4a] Figure 3b displays the RT Raman spectra of the $NdB_6$ nanoneedles (sample **d**). The *Pm-3m* symmetry of the $NdB_6$ structure gives us the following normal lattice vibration modes: $\Gamma = A_{1g}+E_g+T_{1g}+T_{2g}+2T_{1u}+T_{2u}$, where the Raman-active phonons are $A_{1g}$, $E_g$, and $T_{2g}$, two $T_{1u}$ modes are infrared-active, and $T_{1g}$ and $T_{2u}$ are optically inactive. Three peaks located at 680, 1143, and 1273 $cm^{-1}$ can be assigned to the Raman active modes $T_{2g}$, $E_g$ and $A_{1g}$, respectively, of $NdB_6$, and they completely satisfy the polarization selection rule in the cubic symmetry.[23] An extra peaks located at 178 $cm^{-1}$, denoted by an arrow, can be regarded as the vibration of the rare-earth ions in the cage, and can be assigned as the "optical" $T_{1u}$ mode.[24] The mode below 100 $cm^{-1}$ and a broad peak at 1400 $cm^{-1}$, denoted by asterisks, are commonly observed for trivalent and intermediate-valent crystals.[25] The relatively intense and sharp

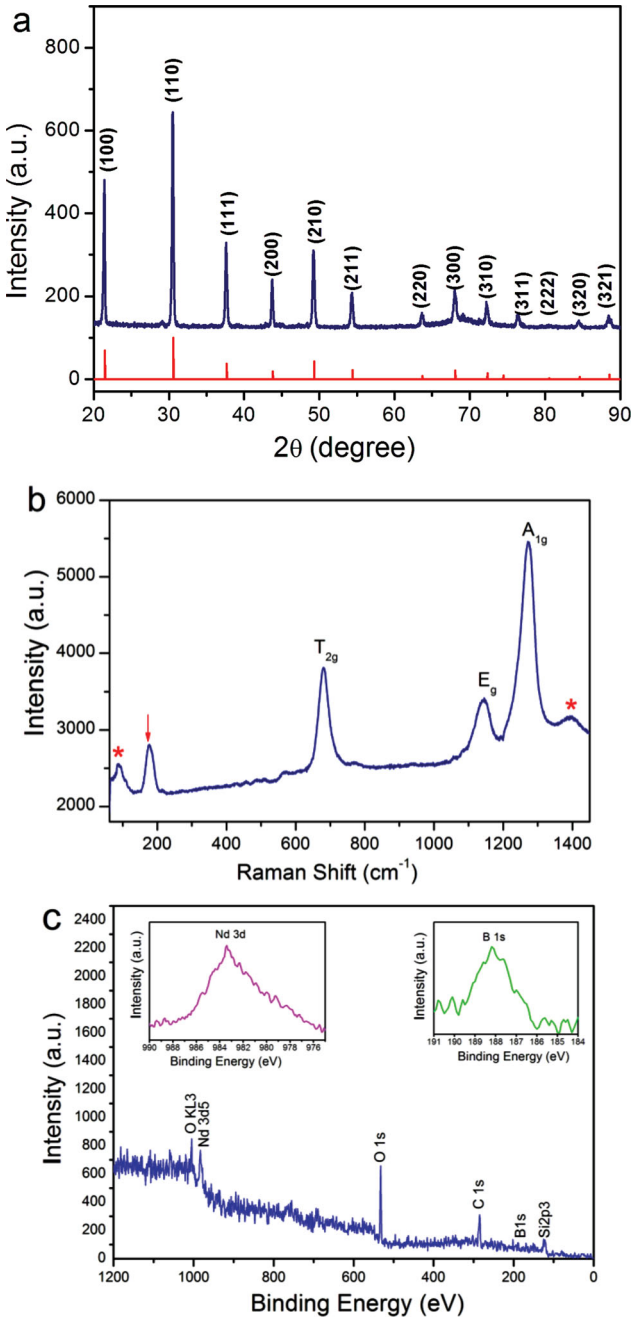


**Figure 3.** (a) XRD pattern of $NdB_6$ nanoneedles; (b) Micro-Raman spectrum of $NdB_6$ nanoneedles at room temperature; (c) Survey spectrum of XPS analysis of $NdB_6$ nanoneedles, and, Nd-3d binding energy spectrum and B-1s binding energy spectrum shown on the left-top and right-top respectively.

peaks suggest that the nanowires are highly crystalline, which is consistent with the XRD pattern and the HRTEM. The $NdB_6$ nanoneedles (sample **d**) have also been further characterized by XPS spectroscopy for the surface analysis. Figure 3c gives the representative spectra, showing that the surface of the sample contains neodymium, boron, carbon and oxygen. The Nd 3d peaks at 983.5 (shown in the top-left of Figure 3c) and B 1s peak at 188.0 eV (shown in top-right **Figure 4**c), agree well with the data obtained in earlier reports[23] and serve as additional confirmation of $NdB_6$ phase.

For the growth of nanostructures in vapor deposition system, two growth mechanisms have been proposed, namely the vapor-solid (VS)[26] and vapor–liquid–solid (VLS).[27] The VLS mechanism can be ruled out here because no metal particles have been found on the tips of the $NdB_6$ nanostructures, thus we suggest that VS mechanism with self-catalyst[28] is dominant. Figure 4 shows schematically the self-catalyst process employed in our experiment together with SEM images of the structures obtained at different reaction times. At the beginning, the Nd atoms generated by thermal evaporation of $NdCl_3$ precursors in vacuum was transported to the Si substrates and decomposed to form Nd nanodroplets (Figures 4$a_1$ and $a_2$). When the $B_2H_6$ was introduced, the B atoms from boron precursor were absorbed by the Nd nanodroplets, resulting in some $NdB_6$ nanoclusters, which, in turn, served as nuclei for the nanowire growth (Figures 4$b_1$ and $b_2$). Subsequently, $NdB_6$ nanowires began to grow and continued as long as appropriate quantities of Nd atoms and B atoms were available (Figures 4$c_1$ and $c_2$). Finally, when heating was stopped, the growth terminated and the $NdB_6$ nanowire formed (Figures 4$d_1$ and $d_2$). Although the time trial growth study does not provide in-situ and in-time vision, the results agree relatively good with the sketch of the overall. Therefore, the growth of $NdB_6$ nanoneedles was attributed to the VS mechanism.

### 2.2. Field-Emission Properties of $NdB_6$ Nanostructures at Room Temperature

FE properties at RT of the as-grown 1D $NdB_6$ nanostructures were studied in this work. So far, to our knowledge, no research on the FE properties of $NdB_6$ nanostructures has been reported. The field emission from the present $NdB_6$ nanostructures was measured at 400 μm gap between the anode and a sample in a vacuum chamber maintained at a pressure of $8.0 \times 10^{-7}$ Pa. The curves of the emission current density versus the applied field (J-E) for the four samples are shown in **Figure 5**, it can be seen that the emission current density J exponentially ascends with the increase of the applied field E. From Figure 5d (sample **d**), the current density reaches 5.37 mA/cm$^2$ at the field of 4.32 V/μm. Such a value is comparable to or even better than those of many other inorganic nanostructures. For example, the emission current density from ZnO nanostructures rarely reaches 1 mA/cm$^2$ at such low electric field unless some special treatments (such as ion implantation and surface modifications) are done, since these nanowires are known to barely sustain such a high current and easily suffer from discharge or breakdown.[29] An emission current density of about 2.1 mA/cm$^2$ was achieved for W nanowires using a similar measurement system, although a lower anode-sample distance of 150 μm was exerted.[30] An emission density of only 0.25 mA/cm$^2$ was observed for CdS nanotips at 10.96 V/μm.[31] Even for $LaB_6$ nanowires, the value of current density can only reach 0.34 mA/cm$^2$ at a filed about 8.1 V/μm under an anode-sample distance of 120 μm.[32] Such a high current density of $NdB_6$ nanoneedles at such a low electric field might be due to the ultra-low work function and large aspect ratio of the $NdB_6$ nanomaterials.

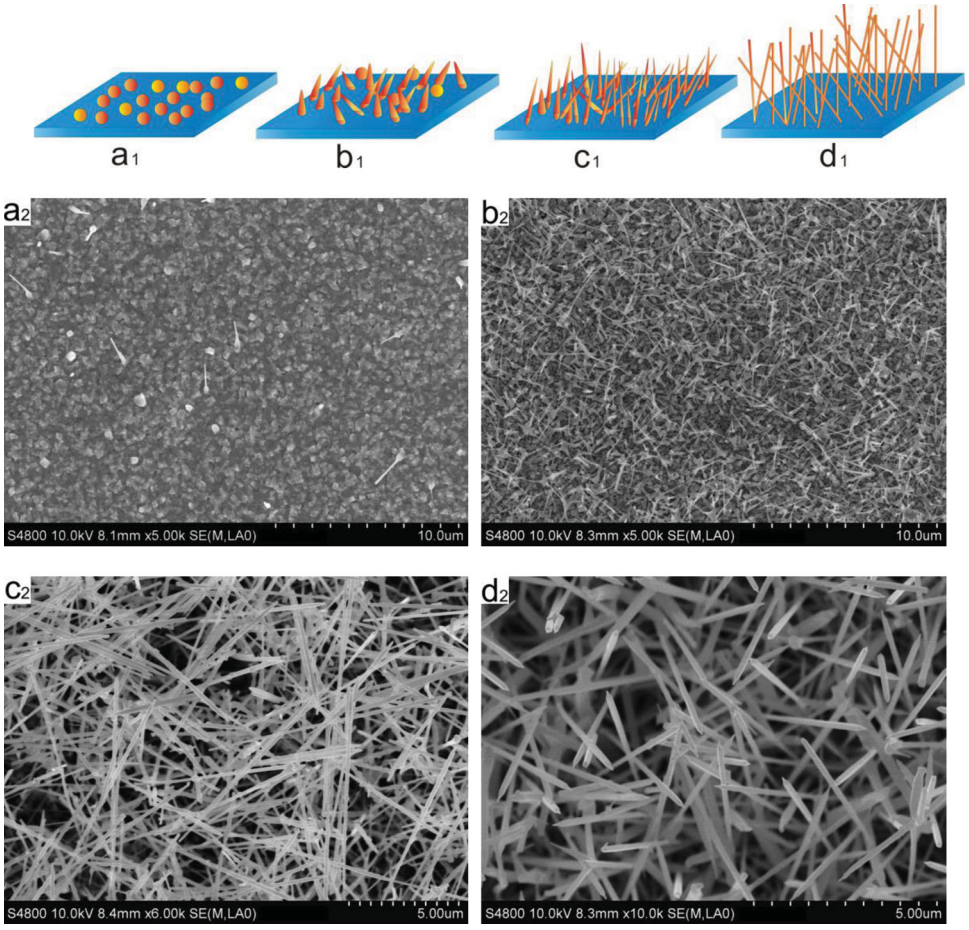


**Figure 4.** ($a_1$–$d_1$) Schematic of the growth procedure of $NdB_6$ nanostructures. SEM images of samples prepared with different growth periods: ($a_2$) 5 min; ($b_2$) 10 min; ($c_2$) 20 min and ($d_2$) 30 min.

Here, we define the turn-on field ($E_{to}$) and threshold field ($E_{thr}$) as the electric fields required producing a current density of 10 μA/cm$^2$ and 1mA/cm$^2$, respectively. As seen from Figure 5, the $NdB_6$ nanoneedles (sample **d**) have the best field emission properties with the lowest turn-on field of 2.71 V/μm and the lowest threshold field of 3.60 V/μm. While the corresponding turn-on fields and threshold fields are 5.60, 3.85, 3.01 V/μm and 7.94, 5.03, 4.31 V/μm for other samples, respectively. From **Table 1**, one can also see that the FE characteristics are morphology-dependent: a curve nanowire (sample **a**) exhibits a poor FE performance due to magnetic field shielding effect, which is often found in SiC nanowires;[33] a long-straight nanowire (sample **c**) shows better FE properties than a short-straight nanorod (sample **b**) due to its larger ratio of length to diameter; for a nanoneedle (sample d), which have sharp tips in comparison with straight nanostructures (sample **b** and **c**) and curve nanowires (sample **a**), demonstrates the best FE performance. These data suggest the NdB6 nanostructures (samples b, c and d) may rival and even surpass those of other inorganic nanostructures for emitter applications (as summarized in **Table 2**).

The FE current-voltage characteristics at RT are further analyzed by a simplified Fowler-Nordheim (F-N) equation[2,45]

$$J = A_E \frac{\beta^2 E^2}{\phi} \exp\left(\frac{-B_E \phi^{3/2}}{\beta E}\right) \quad (1)$$

or

$$\ln\left(\frac{J}{E^2}\right) = \ln\left(\frac{A_E \beta^2}{\phi}\right) - \frac{B_E \phi^{3/2}}{\beta E} \quad (2)$$

Where $A_E = 1.54 \times 10^{-6}$ A eV V$^{-2}$, $B_E = 6.83 \times 10^3$ eV$^{-3/2}$μm$^{-1}$, J is the current density, $\beta$ is the field enhancement factor, E is the applied field, and $\phi$ is the work function of the emitting material, which is 1.6 eV for $NdB_6$. The linear variation of ln ($J/E^2$) vs 1/E (the F-N plots) (the insets of Figure 5) implies that the electron emission from $NdB_6$ nanostructures follows the traditional F-N behavior, i.e. a process of tunneling of electrons through a potential barrier. The calculated field-enhancement factors from the F-N plots are summarized in Table 1. Nanoneedles have the highest $\beta$ value (368), compared to sample **a** (191), sample **b** (220) and sample **c** (305). The higher $\beta$ of sample **d** is thought to profit from its higher aspect ratio and smaller emitter radius than those of sample **a**, **b**, and **c**.

The emission stability behaviors of the $NdB_6$ nanoneedles is also investigated. The representative emission stability curve by keeping an electric field at 3.5 V/μm over a period of 12 hours

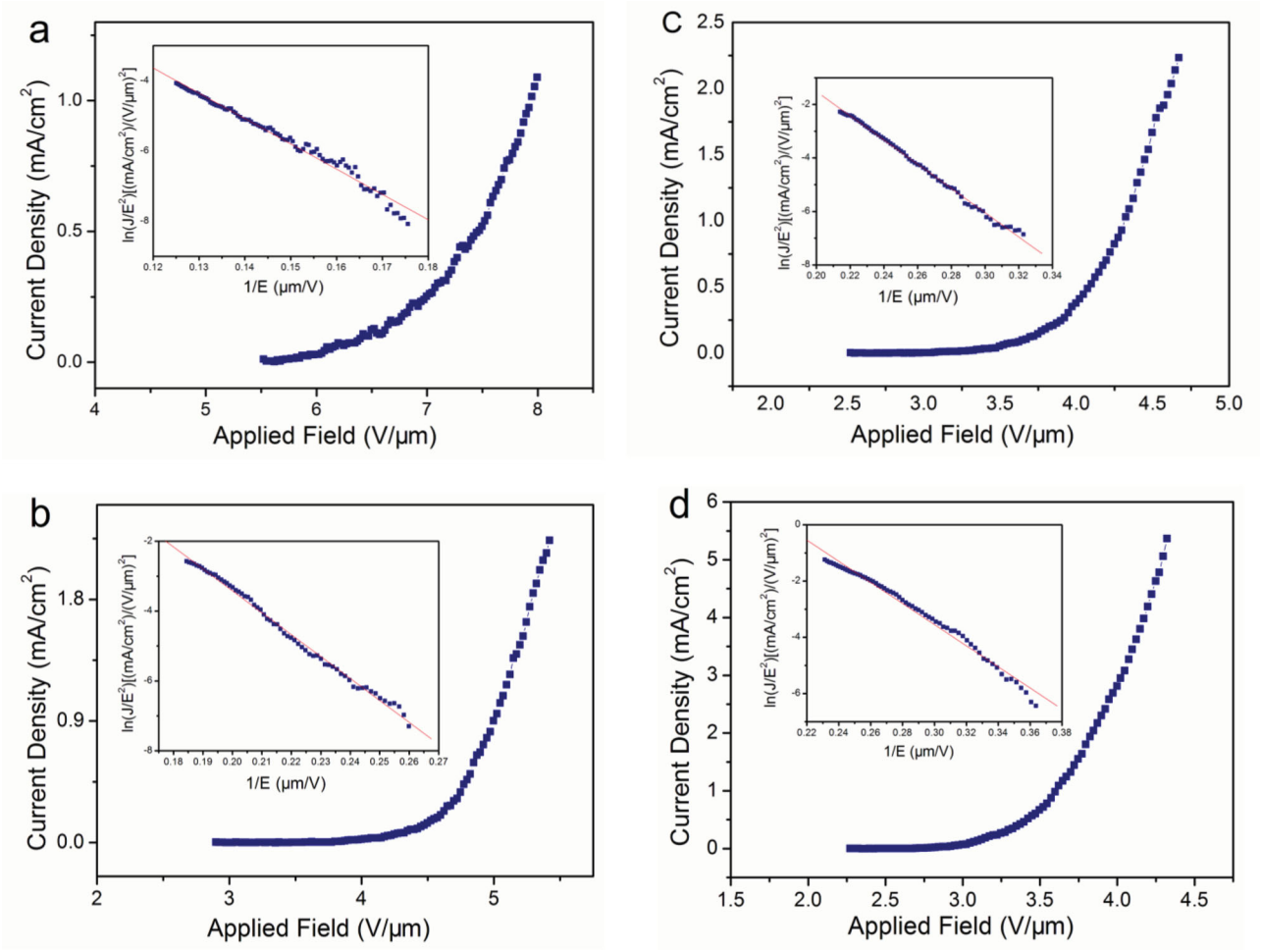


**Figure 5.** Field-emission properties of (a) curve nanowires; (b) short-straight nanorods; (c) long-straight nanowires and (d) nanoneedles. The insets are the corresponding Fowler-Nordheim $\ln(J/E^2)$-(1/E) plots showing linear dependence.

is given in **Figure 6**. No notable current density degradation was observed, and the emission current fluctuations were as low as 5.2%, indicating the high stability of $NdB_6$ nanoneedles. The stable FE performance may be attributed to the uniform distribution of the $NdB_6$ nanoneedles, which guarantees a uniform field emission current across the nanostructures. In comparison, Table 2 summarizes the key performance parameters of some field emitters reported in the literature. The $NdB_6$ nanoneedles are comparable to other nanostructured emitters. Such good field emission may own to the unique characteristics of our $NdB_6$ samples, e.g., ultra-low work function, sharp tips of the nanoneedles, high aspect ratio of length to diameter, high chemical resistance, and high mechanical strength etc.. In comparison with carbon nanotube (CNTs), the relative high turn-on field and low field enhancement factor ($\beta$) of $NdB_6$ nanostructures mainly attribute to the random alignment of these nanoneedles as well as field screen effect caused by higher population density of the emitters. The intrinsic values of the current density and $\beta$ for vertically aligned nanoneedle arrays with appropriate density should probably be much higher than the values obtained in this work, so we suggest precisely control of morphology, alignment, and position should be further studied in future.

**Table 1.** Turn-on fields, threshold fields and field enhancement factors ($\beta$) for the produced $NdB_6$ nanostructures.

| Sample | Morphology | Turn-on field [V μm$^{-1}$] | Threshold field [V μm$^{-1}$] | $\beta$ |
|---|---|---|---|---|
| a | curve nanowires | 5.60 | 7.94 | 191 |
| b | short-straight nanorods | 3.85 | 5.03 | 220 |
| c | long-straight nanowires | 3.01 | 4.31 | 305 |
| d | nanoneedles | 2.71 | 3.60 | 368 |

### 2.3. Temperature-Dependent Field-Emission Properties of $NdB_6$ Nanoneedles

Besides the work function and morphology of the cathode materials, temperature of the cathode is another important factor for the FE performance. Temperature-dependent field electron emission[46,47] can provide deep insight into the physical

**Table 2.** Key field-emission performance parameters of some nanostructured field emitters reported in the literature and in this work.

| Materials | Turn-on field [V μm$^{-1}$] | Threshold field [V μm$^{-1}$] | Field enhancement factor ($\beta$) | Stability: testing time and fluctuation | Ref. |
|---|---|---|---|---|---|
| Carbon nanotube arrays | - | 2.7–3.3 | - | 20 h, - | [34] |
| Layered $MoS_2$ Sheets | 3.5 | | 1138 | 3h, <15% | [35] |
| W nanowire arrays | 4.0 | - | 1904 | 6 h, <3.6% | [30] |
| Mo nanwoires | 5.0 | 9.9 | - | - | [36] |
| Si nansoires | 7.3 | - | 424 | - | [37] |
| $In_2O_3$ nanowires | 10.7 | 17.7 | - | 3h, <10% | [38] |
| ZnO nanowire arrays | 5.6 | 9.3 | 1397 | - | [39] |
| $WO_3$ nanostructures | 6.2 | - | 1480 | - | [40] |
| ZnS nanowires | 5.5–11.67 | - | 1942–891 | 8 h, - | [41] |
| CdS nanowires | 8.95 | 10.39 | 388 | 1000 min, - | [31] |
| SiC nanotubular | 5 | 10 | - | - | [42] |
| AlN nanotips | 4.7 | - | 1175.5 | 4h, <0.74 | [43] |
| $LaB_6$ nanorods | 4.62 | - | 405 | 10 h, <10% | [32] |
| $CeB_6$ nanorods | 9.5 at 0.1 μA cm$^{-2}$ | - | 1035–1165 | 2.2 h, <10% | [44] |
| $NdB_6$ nanoneedles | 2.71 | 3.60 | 368 | 12 h, <5.2% | This work |
| long-straight $NdB_6$ nanowires | 3.01 | 4.31 | 305 | - | This work |
| short-straight $NdB_6$ nanorods | 3.85 | 5.03 | 220 | - | This work |

properties of a nanostructure, reveal the relations between the electron emission characteristics and temperature conditions, and help understanding the direct thermal electric conversion. Recently, many efforts have been devoted to study the temperature-dependent FE of CNTs,[46,48] ZnO nanowires,[47] AlN nanotips,[49] graphene films,[50] SiC nanostructures,[51] etc.; all the authors got similar results: Higher the temperature of emitter is, more decrease the turn-on and threshold electric fields. However, no research on high temperature field emission of $NdB_6$ nanoneedles has yet been initiated, so the investigation of temperature-dependent field emitters of $NdB_6$ arrays is highly needed.

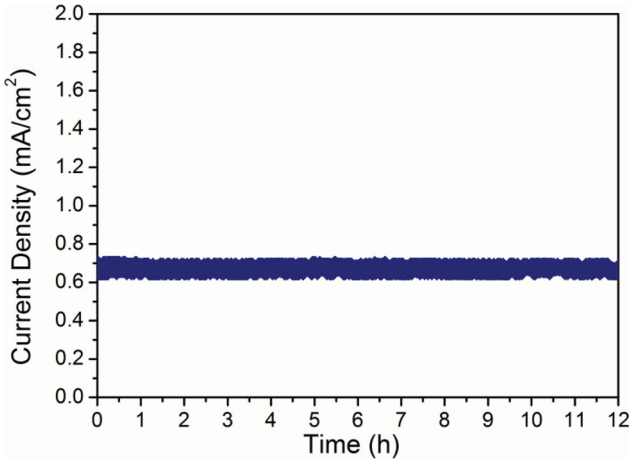


**Figure 6.** Representative stability curve of $NdB_6$ nanoneedles at RT.

Normally, for temperature dependent field emission, the total current density J is given by simplified F-N equation and Richardson equation as:[48,52]

$$J = J_E + J_T = \frac{A_E \beta^2 E^2}{\phi} \exp\left(\frac{-B_E \phi^{3/2}}{\beta E}\right)\left[\frac{\theta}{\sin(\theta)}\right] + A_R T^2 e^{-\phi/kT} \quad (3)$$

$$\theta \approx \frac{2.2\pi(kT/q)\phi^{1/2}}{1.959E} \quad (4)$$

Where $J_E$ is the field current density, $J_T$ is thermionic current density, $A_R$ is Richardson constant with a theoretical value of 120 A vm$^{-2}$ K$^{-2}$, T is the emitter temperature, k is the Boltzmann constant, and $\theta$ is the temperature correction factor ($A_E$, $B_E$, J, $\beta$, and E are defined as before). Specific to $NdB_6$ with a work function of 1.6 eV and temperature below 1000 K, the value of $[\frac{\theta}{\sin(\theta)}]$ is always 1.0 within the studied temperature range. Therefore, the contribution of thermionic emission to the current density is much smaller than FE. And the temperature-dependent field emission characteristics can be expressed by the traditional F-N Equation (3) and (4).

**Figure 7**a shows the characteristic J-E curves of $NdB_6$ nanoneedle emitters at different temperatures with an anode-sample distance of 400 μm. It was observed that the emission current density is dependent on a number of factors, the applied field, tip geometry, cathode work function, emission temperature, etc., variations in any of these factors would be reflected in the emission currents. The relatively smooth and consistent curve of the sample at the excitation of thermal field indicates the stable electron emission. When the temperature increases from RT to 623 K, it is very interesting that the turn-on field

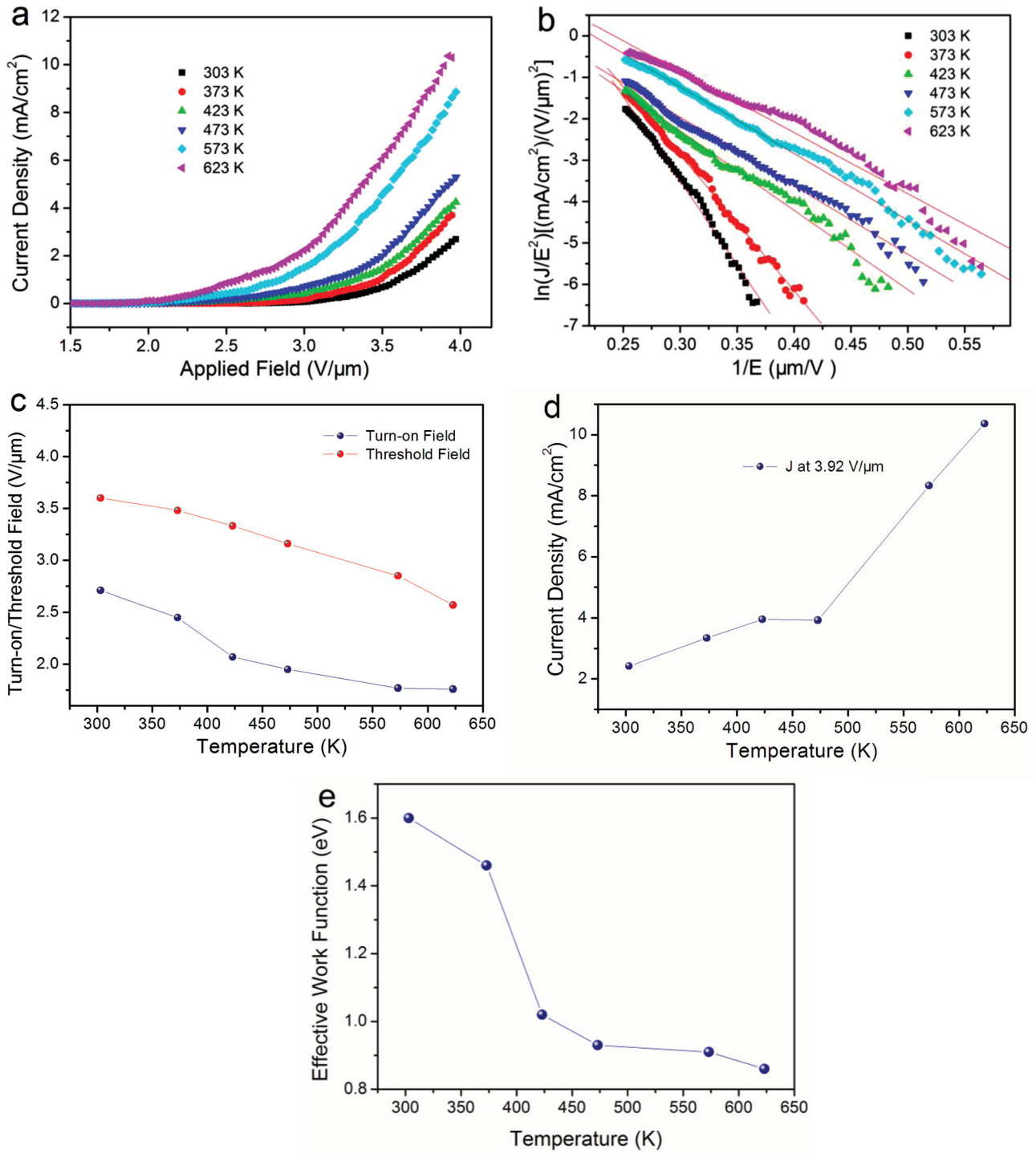


**Figure 7.** Dependence of field emission current J on the applied electric field E of $NdB_6$ nanoneedles at different temperatures: (a) J-E plots; (b) The F-N plots for different temperatures; (c) Turn-on field and threshold field at different temperatures; (d) Variations of emission current at 3.92 V $\mu m^{-1}$ at different temperature; (e) Work function at ambient temperature.

and threshold field of the sample decreases rapidly from 2.71 to 1.76 and 3.60 to 2.57 V/μm, respectively, as shown in Figures 7a and c. Meanwhile, at an applied electric field of 3.92 V/μm the emission current density increases significantly from 2.42 to 10.36 mA/cm$^2$, shown in Figures 7a and d. In other words, to obtain an emission of 2 mA/cm$^2$, the required electric field for this $NdB_6$ nanoneedle emiter is 3.85 V/μm at RT but 2.95 V/μm at 623 K. The current density of $NdB_6$ nanoneedles (10.36 mA/cm$^2$ under a field of 3.92 V/μm at 623 K) is apparently better than those of other temperature-dependent field

**Table 3.** Key temperature-dependent field-emission performance parameters of some nanostructured field emitters reported in the literature and in this work.

| Materials | Turn-on field at RT [V/μm] | Threshold field at RT [V/μm] | whether linear relation between ln(J/E$^2$) and 1/E | Maxim J at corresponding E and T [mA/cm$^2$; V/μm; K] | Ref. |
|---|---|---|---|---|---|
| Carbon nanotubes | 7.5 | - | Yes | 0.3; 8.3; 573 | [46] |
| multiwalled carbon nanotubes | - | 4.0 | Yes | 9.6; 8.9; 650 | [48] |
| graphene film | 9.8 | - | Yes | 0.2;7.6; 623 | [50] |
| ZnO nanorods | 7.5 | 15 | Yes | 3.2;6.0; 600 | [47] |
| AlN nanotips | 7.7 | 7.9 | Yes | 1.0; 4.5; 573 | [49] |
| $LaB_6$ nanowires | 4.6 | - | Yes | 2.7; 8.2; 573 | [32] |
| $NdB_6$ nanoneedles | 2.71 | 3.60 | Yes | 10.3; 3.94; 623 | This work |

emitters (as summarized in **Table 3**), which promises a good future of this $NdB_6$ nanostructure in practical field emitter applications.

The decrease of turn-on field and increase of emission current density upon the increase of temperature might be a result of the decrease of effective work function of the $NdB_6$ nanoneedle emitters. Further analysis on the temperature-dependent FE properties of $NdB_6$ nanoneedles were done by using Fowler-Nordheim theory described in Equation (4). In the range of RT to 623 K, the linear relationship indicates that the field-emission behavior obeys the FN rule as the electrons can tunnel through the potential barrier from conduction band to vacuum. As a matter of fact that the change of temperature between RT and 623 K will not influence the crystal structure, emitter geometry, and spatial distribution of emitting centers, field-enhancement factor ($\beta$) should be a constant in the test range of temperatures. To estimate the effective work function ($\Phi$) of these $NdB_6$ nanoneedles, we assume the initial $\Phi$ at RT is 1.6 eV, and $\beta$ of the $NdB_6$ nanoneedles is 368 from the constant F-N slope. Assuming that $\beta$ does not change with temperature, then the effective work function ($\Phi_{eff}$) at different temperature can be calculated through the relation $k = -B\Phi_{eff}^{3/2}/\beta$. From Figure 7e, the $\Phi_{eff}$ decreases from 1.60 to 0.86 eV with the increase of temperature, which interprets well the temperature-dependent field-emission effects for the $NdB_6$ nanoneedles: the significant reduction of the turn-on field and the remarkable increase of emission current result from the sharp decrease of work function at increased temperature.

To date, Temperature-dependent FE characteristics of the nanostructures have not been completely understood. Although the exact explanation of the observed temperature dependence of the emission current needs more research, the following effects may have strong influence. As known, the $NdB_6$ is a semiconductor materials, and in physical, the work function ($\Phi$) can be expressed as:[53,54]

$$E_F = E_0 - E_F \tag{5}$$

$$E_F = \frac{E_C + E_V}{2} + \frac{k_B}{2} T \ln \frac{N_V}{N_C} \tag{6}$$

Where $E_0$ is the fixed vacuum level, $E_F$ is the Femi energy, $E_C$ is the conduction band energy, $E_V$ is the valence band energy, $k_B$ is the Boltzmann constant, T is the temperature, $N_V$ and $N_C$ are the effective density-of-state of electron and holes, respectively. Specific to the $NdB_6$ nanoneedles, at low temperature Femi energy is lower, the barrier height is also larger and electrons tunneling probability decreases; with temperature increase, Femi energy also increases, the barrier (i.e. effective work function) decreases from 1.60 to 0.86 eV (as shown in Figure 7e). Therefore, the turn-on and threshold fields decrease (shown in Figure 7c), while the field emission current increases (as shown in Figure 7d) when the temperature is elevated. Such phenomen have also been found in other semiconductor materials, such as CNTs,[44] graphene film,[46] ZnO nanoarrays[43] and SiC nanoneedles,[48,49] in which the enhanced FE properties are attributed to the rising of Fermi level along temperature.

## 3. Conclusions

High-quality $NdB_6$ nanostructures with low work function were successfully synthesized via an one-step catalyst-free chemical vapor deposition process. Through tuning the reaction temperatures and the distances between the precursors and the substrate, the morphologies of $NdB_6$ nanostructures can be changed from curve nanowires, short-straight nanorods, long-straight nanowires to nanoneedles. Field emission measurements at room temperature show that the field-emission performance relies not only on aspect-ratio (length to the diameter) but also on the detailed morphology (such as nanowires of curve or straight axial). Among the four samples, the nanoneedles exhibit the best field emission behaviors: the turn-on and the threshold electric fields are as low as 2.71 and 3.60 V/μm, respectively, with a good stability. The excellent performance is believed to benefit from ultra-low work function, sharpened tips, and straight morphology. Field emission of $NdB_6$ nanoneedles at various temperatures are first reported in this study. It is found that the turn-on and threshold electric fields decrease from 2.71 to 1.76, from 3.60 to 2.57 V/μm, respectively, when the temperature increases from RT to 623 K. The work function of $NdB_6$ nanoneedles is dramatically reduced along with the increasing temperature, leading to much improved field emission properties. $NdB_6$ nanostructures, with good electrical transport and field emission properties, may serve as promising candidates for application in flat panel displays and nanoelectronics building blocks.

**Table 4.** Growth conditions for 1D $NdB_6$ nanostructures

| Sample | Si substrates | Catalysts | Distance between source and substrates [cm] | T [°C] | t [min] | Reaction pressure [Pa] | Wash gas: ratio of $H_2$/Ar and flow [sccm] | Reaction gas: ratio of $H_2$/$B_2H_6$ and flow [sccm] |
|---|---|---|---|---|---|---|---|---|
| **a** | <100> | no | 3 | 860 | 30 | ~15 | 3:7; 100 | 1:19; 50 |
| **b** | <100> | no | 5 | 880 | 30 | ~15 | 3:7; 100 | 1:19; 50 |
| **c** | <100> | no | 7 | 900 | 30 | ~15 | 3:7; 100 | 1:19; 50 |
| **d** | <100> | no | 9 | 920 | 30 | ~15 | 3:7; 100 | 1:19; 50 |

## 4. Experimental Section

$NdB_6$ nanostructures were prepared by a catalyst-free chemical vapor deposition (CVD) method as shown in Figure S2 (see Supporting Information). In brief, the synthesis is based on the following chemical reactions:

$$NdCl_3 \cdot 6H_2O(s) \longrightarrow NdCl_3(s) + H_2O(g)$$

$$NdCl_3(s) + B_2H_6(g) \longrightarrow NdB_6(s) + HCl(g) + Cl_2(g)$$

The reaction was conducted in a horizontal quartz tube furnace. In a typical run, 0.2 g neodymium chloride hexahydrate ($NdCl_3 \cdot 6H_2O$; mass purity: 99.9%) was loaded near the closed end of the quartz test tube and deposited in the uniform temperature region, while Si wafers were placed upstream to act as deposition substrates. Prior to heating, the quartz tubes were evacuated and washed with a mixed gas (30%$H_2$+70%Ar; volume percent calculation). After that, the quartz tube was heated to a preset furnace temperature with an heating rate of ~15 °C/min while pumping vacuum. Then a steady mixed gas (5% $B_2H_6$+95% Ar) about 50 sccm was flowed over 30 min under the reaction pressure of ~15 Pa. After the reaction, the furnace was cooled down to room temperature under vacuum within 5 h. Four representative samples (a, b, c and d) were fabricated by varying some experimental parameters, the detailed growth conditions are listed in **Table 4**.

The synthesized products were characterized by a scanning electron microscopy (Hitachi S4800), X-ray diffraction (D8/advance), Raman spectrometry (Horiba Jobin-Yoon T6400), transmission electron microscopy (JEM-3000F), and X-ray energy dispersive spectrometry. X-ray photoelectron spectra were measured using an ESClab-220i-XL electron spectrometer (VG Scientific) using 300 W Al Kα radiations. The field-emission properties were analyzed on a home-built parallel-plate-electrode high vacuum field emission system with a base pressure of ~$8.0 \times 10^{-7}$ Pa at different controlled temperatures. The distance between the substrate surface and the anode of vacuum chamber was fixed at 400 μm.

## Supporting Information

Supporting Information is available from the Wiley Online Library or from the author.

## Acknowledgements

This work was supported by the National 1000 Talents Program of China tenable in Huazhong University of Science and Technology (HUST), the National Nature Science Foundation of China (11004167, 21273249), Program for Science & Technology Innovation Talents in Universities of Henan Province (13HASTIT047), and the Academic Excellent Young Teachers Program of Henan Province (2011GGJS-121).

Received: June 10, 2013
Revised: June 24, 2013
Published online: August 21, 2013

[1] a) T. Y. Zhai, J. N. Yao, *One-Dimensional Nanostructrues: Principles and Applications*, John Wiley & Sons, Inc., Hoboken, USA **2013**; b) T. Zhai, L. Li, Y. Ma, M. Liao, X. Wang, X. Fang, J. Yao, Y. Bando, D. Golberg, *Chem. Soc. Rev.* **2011**, *40*, 2986; c) X. H. Zhang, L. Gong, K. Liu, Y. Z. Cao, X. Xiao, W. M. Sun, X. J. Hu, Y. H. Gao, J. Chen, J. Zhou, Z. L. Wang, *Adv. Mater.* **2010**, *22*, 5292; d) H. J. Jeong, H. D. Jeong, H. Y. Kim, J. S. Kim, S. Y. Jeong, J. T. Han, D. S. Bang, G. W. Lee, *Adv. Funct. Mater.* **2011**, *21*, 1526; e) J. T. H. Tsai, T. Y. E. Chu, J. Y. Shiu, C. S. Yang, *Small* **2012**, *8*, 3739; f) Z. Li, L. N. Cheng, Q. Sun, Z. H. Zhu, M. J. Riley, M. Aljada, Z. X. Cheng, X. L. Wang, S. Z. Qiao, S. C. Smith, G. Q. Lu, *Angew. Chem. Int. Ed.* **2010**, *49*, 2777; g) H. Q. Li, X. Wang, J. Q. Xu, Q. Zhang, Y. Bando, D. Golberg, Y. Ma, T. Y. Zhai, *Adv. Mater.* **2013**, *25*, 3017.

[2] R. H. Fowler, L. W. Nordheim, *Proc. R. Soc. London A* **1928**, *119*, 173.

[3] J. M. Lafferty, *Appl. Phys.* **1951**, *22*, 299.

[4] a) S. S. Kher, J. V. Romero, J. D. Caruso, J. T. Spe, *Appl. Organometal. Chem.* **2008**, *22*, 300; b) S. S. Kher, J. T. Spencer, *J. Phys. Chem. Solids* **1998**, *59*, 1343.

[5] M. Nakamoto, K. Furuda, *Appl. Surf. Sci.* **2002**, *202*, 289.

[6] D. J. Late, M. A. More, P. Misra, B. N. Singh, L. M. Kukreja, D. S. Joag, *Ultramicroscopy* **2007**, *107*, 825.

[7] a) H. Zhang, Q. Zhang, G. P. Zhao, J. Tang, O. Zhou, L. C. Qin, *J. Am. Chem. Soc.* **2005**, *127*, 8002; b) H. Zhang, Q. Zhang, G. P. Zhao, J. Tang, O. Zhou, L. C. Qin, *J. Am. Chem. Soc.* **2005**, *127*, 13120; c) H. Zhang, J. Tang, Q. Zhang, G. P. Zhao, G. Yang, J. Zhang, O. Zhou, L. C. Qin, *Adv. Mater.* **2006**, *18*, 87.

[8] a) J. Q. Xu, Y. M. Zhao, C. Y. Zou, *Chem. Phys. Lett.* **2006**, *423*, 138; b)Q. Y. Zhang, J. Q. Xu, Y. M. Zhao, X. H. Ji, S. P. Lau, *Adv. Funct. Mater.* **2009**, *19*, 742.

[9] K. C. Qi, Z. L. Lin, W. B. Chen, G. C. Cao, J. B. Cheng, X. W. Sun, *Appl. Phys. Lett.* **2008**, *93*, 093503.

[10] a) J. R. Brewer, N. Deo, M. Y. Wang, C. L. Cheung, *Chem. Mater.* **2007**, *19*, 6379; b) J. R. Brewer, R. M. Jacobberger, D. R. Diercks, C. L. Cheung, *Chem. Mater.* **2011**, *23*, 2606.

[11] M. F. Zhang, Y. Jia, G. G. Xu, P. F. Wang, X. Q. Wang, S. L. Xiong, X. J. Wang, Y. T. Qian, *Eur. J. Inorg. Chem.* **2010**, *8*, 1289.

[12] V. Semet, C. Adessi, T. Capron, R. Mouton, V. T. Binh, *Phys. Rev. B* **2007**, *75*, 45430.

[13] P. H. Schmidt, L. D. Longinotti, D. C. Joy, S. D. Ferris, H. J. Leamy, Z. Fisk, *J. Vac. Sci. Technol.* **1978**, *15*, 1554.

[14] T. B. Massalski, *Binary Alloy Phase Diagrams*, ASM International: Materials Park, OH, USA **1990**, Vol. *2*.

[15] A. Tanaka, K. Tamura, K. Takahashi, M. Hatano, T. Okane, S. Suzuki, S. Sato, S. KuniP, A. Harasawa, A. Kimura, A. Kakizaki, *Physica B* **1997**, *240*, 123.

[16] Y. F. Yuan, L. Zhang, L. M. Liang, K. He, R. Liu, G. H. Min, *Ceram. Int.* **2011**, *37*, 2891.

[17] M. Jha, R. Patra, S. Ghosh, A. K. Ganguli, *J. Mater. Chem.* **2012**, *22*, 6356.

[18] J. Q. Xu, T. Mori, Y. Bando, D. Golberg, D. Berthebaud, A. Prytuliak, *Mater. Sci. Eng. B* **2012**, *177*, 117.

[19] M. F. Zhang, L. Yuan, X. Q. Wang, H. Fan, X. Y. Wang, X. Y. Wu, H. Z. Wang, Y. T. Qian, *J. Solid State Chem.* **2008**, *181*, 294.
[20] Q. W. Ding, Y. M. Zhao, J. Q. Xu, C. Y. Zou, *Solid State Commun.* **2007**, *141*, 53.
[21] G. H. Wang, J. R. Brewer, J. Y. Chan, D. R. Diercks, C. L. Cheung, *J. Phys. Chem. C* **2009**, *113*, 10446.
[22] J. Q. Xu, G. H. Hou, H. Q. Li, T. Y. Zhai, B. P. Dong, H. L. Yan, Y. R. Wang, B. H. Yu, Y. Bando, D. Golberg, *NPG Asia Mater.* **2013**, doi: 10.1038/am.2013.25.
[23] R. K. Selvan, I. Genish, I. Perelshtein, J. M. C. Moreno, A. Gedanken, *J. Phys. Chem. C* **2008**, *112*, 1795.
[24] N. Ogita, S. Nagai, N. Okamoto, M. Udagawa, F. Iga, M. Sera, J. Akimitsu, S. Kunii, *Phys. Rev. B* **2003**, *68*, 224305.
[25] N. Ogita, S. Nagai, M. U. Dagawa, F. Iga, M. Sera, T. Oguchi, J. Akimitsu, S. Kunii, *Physica B* **2005**, *359*, 941.
[26] Y. N. Xia, P. D. Yang, Y. G. Sun, Y. Y. Wu, B. Mayer, B. Gates, Y. D. Yin, F. Kim, Y. Q. Yan, *Adv. Mater.* **2003**, *15*, 353.
[27] Z. W. Pan, Z. R. Dai, Z. L. Wang, *Science* **2001**, *291*, 1947.
[28] H. Y. Dang, J. Wang, S. S. Fan, *Nanotechnology* **2003**, *14*, 738.
[29] a) J. C. She, Z. M. Xiao, Y. H. Yang, S. Z. Deng, J. Chen, G. W. Yang, N. S. Xu, *ACS Nano* **2008**, *2*, 2015; b) Q. Zhao, J. Y. Gao, R. Zhu, T. C. Cai, S. Wang, X. S. Song, Z. M. Liao, X. H. Chen, D. P. Yu, *Nanotechnology* **2010**, *21*, 095701; c) C. H. Ye, Y. Bando, X. S. Fang, G. Z. Shen, D. Golberg, *J. Phys. Chem. C* **2007**, *111*, 12673.
[30] S. L. Wang, Y. H. He, X. S. Fang, J. Zou, Y. Wang, H. Huang, P. M. F. J. Costa, M. Song, B. Y. Huang, C. T. Liu, P. K. Liaw, Y. Bando, D. Golberg, *Adv. Mater.* **2009**, 21, 2387.
[31] T. Y. Zhai, X. S. Fang, Y. Bando, B. Dierre, B. D. Liu, H. B. Zeng, X. J. Xu, Y. Huang, X. L. Yuan, T. Sekiguchi, D. Golberg, *Adv. Funct. Mater.* **2009**, *19*, 2423.
[32] J. Q. Xu, Y. M. Zhao, Q. Y. Zhang, *J. Appl. Phys.* **2008**, *104*, 124306.
[33] Z. J. Li, W. P. Ren, A. L. Meng, *Appl. Phys. Lett.* **2010**, *97*, 263117.
[34] S. S. Fan, M. G. Chapline, N. R. Franklin, T. W. Tombler, A. M. Cassell, H. J. Dai, *Science* **1998**, *283*, 512.
[35] R. V. Kashid, D. J. Late, S. S. Chou, Y. K. Huang, M. D. Dilip, S. Joag, M. A. More, V. P. Dravid, *Small* **2013**, DOI: 10.1002/smll.201300002.
[36] J. Zhou, S. Z. Deng, L. Gong, Y. Ding, J. Chen, J. X. Huang, J. Chen, N. S. Xu, Z. L. Wang, *J. Phys. Chem. B* **2006**, *110*, 10296.
[37] X. S. Fang, Y. Bando, C. H. Ye, G. Z. Shen, U. K. Gautam, C. C. Tang, D. Golberg, *Chem. Commun.* **2007**, *40*, 4093.
[38] S. Q. Li, Y. X. Liang, T. H. Wang, *Appl. Phys. Lett.* **2006**, *88*, 053107.
[39] Z. Q. Wang, J. F. Gong, Y. Su, Y. W. Jiang, S. G. Yang, *Cryst. Growth Des.* **2010**, *10*, 2455.
[40] a) J. Zhou, Y. Ding, S. Z. Deng, L. Gong, N. S. Xu, Z. L. Wang, *Adv. Mater.* **2005**, *17*, 2107; b) M. T. Chang, L. J. Chou, Y. L. Chueh, Y. C. Lee, C. H. Hsieh, *Small* **2007**, *3*, 3463; c) F. Liu, F. Y. Mo, S. Y. Jin, L. Li, Z. S. Chen, R. Sun, J. Chen, S. Z. Deng, N. S. Xu, *Nanoscale* **2011**, *3*, 1850.
[41] M. Hafeez, T. Y. Zhai, A. S. Bhatti, Y. Bando, D. Golberg, *J. Phys. Chem. C* **2012**, *116*, 8297.
[42] H. Cui, Y. Sun, G. Z. Yang, J. Chen, D. Jiang, C. X. Wang, *Chem. Commun.* **2009**, *41*, 6243.
[43] Y. B. Tang, H. T. Cong, Z. G. Cheng, *Appl. Phys. Lett.* **2005**, *86*, 233104.
[44] M. Jha, R. Patra, S. Ghosh, A. K. Ganguli, *J. Mater. Chem.* **2012**, *22*, 6356.
[45] J. G. Liu, Z. J. Zhang, Y. Zhao, X. Su, S. Liu, E. G. Wang, *Small* **2005**, *1*, 310.
[46] M. C. Kan, J. L. Huang, J. C. Sung, K. H. Chen, B. S. Yau, *Carbon* **2003**, *41*, 2839.
[47] L. Liao, W. F. Zhang, H. B. Lu, J. C. Li, D. F. Wang, C. Liu, D. J. Fu, *Nanotechnology* **2007**, *18*, 225703.
[48] S. F. Ahmed, S. Das, M. K. Mitra, K. K. Chattopadhyay, *Appl. Sur. Sci.* **2007**, *254*, 610.
[49] X. H. Ji, Q. Y. Zhang, S. P. Lau, H. X. Jiang, J. Y. Lin, *Appl. Phys. Lett.* **2009**, *94*, 173106.
[50] J. Li, J. T. Chen, B. S. Shen, X. B. Yan, Q. J. Xue, *Appl. Phys. Lett.* **2011**, *99*, 163103.
[51] M. Choueib, M. Ayari, P. Vincent, K. Bachelany, D. Cornu, S. Purcell, *Phys. Rev. B* **2009**, *79*, 075421.
[52] A. Modinos, *Field, Thermionic, and secondary Electron Emission Spectroscopy*, Plenum, New York, USA **1984**.
[53] M. A. Uijttewaal, G. A. de Wijs, R. A. de Groo, *J. Phys. Chem. B* **2006**, *110*, 18459.
[54] S. M. Sze, *Semiconductor Devices: Physics and Technology*, Wiley, India **2009**.